Supporting Information for

How urban heterogeneity and turbulence shape street-level heat exposure

Fytanidis et al.

Dimitrios K. Fytanidis.
E-mail: dfytanidis@anl.gov

This PDF file includes:

Supporting Information Text

A1. Derivation and Correspondence between ℓ and ℓ_ε. In Santiago and Martilli (1), the dissipation mixing length ℓ_ε, formulation is defined via the relation $C_k\ell = C_\mu \frac{\ell_\varepsilon}{C_\varepsilon}$, where $C_\mu = 0.09$, $C_k = 0.4$, and $C_\varepsilon = 0.71$ (1). Their equations (16a–c) therefore define ℓ_ε (normalized by H) as:

$$\frac{\ell_\varepsilon}{C_\varepsilon H} = \begin{cases} \alpha_1' \left(1 - \frac{d}{H}\right), & z \le H \\ \alpha_1' \left(\frac{z}{H} - \frac{d}{H}\right), & H < z \le 1.5H \\ \alpha_2' \left(\frac{z}{H} - \frac{d_2}{H}\right), & z > 1.5H \end{cases} \quad [A1]$$

To convert these expressions into a mixing length form ℓ, one substitutes into the dimensional relationship above:

$$\frac{\ell}{H} = C_\mu \frac{\ell_\varepsilon}{C_\varepsilon C_k} = \begin{cases} \alpha_1 \frac{C_\mu}{C_\varepsilon C_k} \left(1 - \frac{d}{H}\right), & z \le H \\ \alpha_1 \frac{C_\mu}{C_\varepsilon C_k} \left(\frac{z}{H} - \frac{d}{H}\right), & H < z \le 1.5H \\ \alpha_2 \frac{C_\mu}{C_\varepsilon C_k} \left(\frac{z}{H} - \frac{d_2}{H}\right), & z > 1.5H \end{cases} \quad [A2]$$

Thus, the coefficient a_1 in the classical mixing length formulation is given by:

$$\alpha_1' = \frac{C_\mu}{C_k}\alpha_1 = \frac{0.09}{0.71} \approx 0.225\alpha_1 \quad [A3]$$

This yields a consistent mapping between the two formulations: reported values of α_1' in the range 0.35–0.71 correspond to $\alpha_1 \approx 1.92$–2.24, as used in the present study. Table S1 summarizes the reported values of α_1 and α_1' along with the corresponding values of ℓ/H and ℓ_ε/H as found in Santiago and Martilli (1), Simón-Moral et al. (2) and Nazarian et al. (3).

Table S1. Reported values of mixing length parameters a_1 and a_1' and the dissipation-based counterparts ℓ/H and ℓ_ε/H.

Study	α_1	α_2	α_1'	α_2'
Santiago and Martilli (1) – RANS	$2.24 - 2.25(2.24)$	$0.98 - 1.12(1.12)$	$0.504 - 0.506(0.504)$	$0.221 - 0.252(0.25)$
Simón-Moral et al. (2014) – RANS	$1.92 - 2.46(2.19)$	$1.14 - 1.27(1.2)$	$0.430 - 0.554(0.492)$	$0.257 - 0.286(0.27)$
Nazarian et al. (2020) – LES	4.0	$min(1.125, \max(0.45, 0.2925))$	0.5*	$min(0.14, \max(0.056, 0.04))$*

*For consistency, a constant value of C_μ was assumed. However, Nazarian et al. (2020) proposed a variable formulation for a_1' as a function of plan area density λ_p defined as $C_\mu \begin{cases} max(0.5, -\lambda^2 + 0.75\lambda_p + 0.022), & z \ge H \\ 0.05, & z < H \end{cases}$.

A2. Averaging Methodologies: Intrinsic vs. Comprehensive Averaging

In building-resolving simulations of urban canopy flows, turbulent quantities must be horizontally averaged to derive representative vertical profiles usable in urban canopy models. Two primary horizontal averaging approaches are:

- **Intrinsic averaging**: averages over the *fluid volume only*.
- **Comprehensive averaging**: averages fluid quantities but normalizes over the *total volume*, including buildings.

A.2.1 Intrinsic Averaging. The intrinsic horizontal average of a scalar variable ϕ is defined as (4, 5):

$$\langle\phi\rangle_I(z) = \frac{1}{A_a(z)} \int_{A_a(z)} \phi(x, y, z)\, dx\, dy \quad [A4]$$

where $A_a(z)$ is the horizontal fluid area at height z.

Applying the spatial averaging theorem (5, 6), the derivative becomes:

$$\left\langle \frac{\partial \phi}{\partial x_i} \right\rangle_I = \frac{\partial \langle\phi\rangle_I}{\partial x_i} + \langle\phi\rangle_I \frac{\partial \epsilon}{\partial x_i} + \frac{1}{A_a} \oint_{\partial A_a} \phi\, n_i\, dl \quad [A5]$$

where $\epsilon(z) = 1 - \lambda_p(z)$ is the local fluid fraction and n_i is the component of the unit normal vector at the fluid–solid interface.

A.2.2 Comprehensive Averaging. The comprehensive average is defined as:

$$\langle \phi \rangle_C(z) = \frac{1}{A} \int_{A_a(z)} \phi(x, y, z)\, dx\, dy \quad [A6]$$

with $A = A_a(z) + A_p(z)$ the total horizontal area. The corresponding derivative is:

$$\left\langle \frac{\partial \phi}{\partial x_i} \right\rangle_C = \frac{\partial \langle \phi \rangle_C}{\partial x_i} + \frac{1}{A} \oint_{\partial A_a} \phi\, n_i\, dl \quad [A7]$$

Unlike intrinsic averaging, the comprehensive approach does not include a $\partial\epsilon/\partial x_i$ term because the averaging volume does not vary with height.

Implications and Application.

- For **horizontal derivatives**, correction terms often vanish under horizontal homogeneity and no-slip conditions.
- For **vertical derivatives**, the correction terms are non-negligible, especially the $\partial\epsilon/\partial z$ term in intrinsic averaging, which accounts for vertical changes in solid fraction.
- The interface integral accounts for discontinuities at building surfaces (e.g., pressure) and is generally zero for velocity under no-slip conditions.

In this study, we adopt **intrinsic averaging** for all velocity, flux, and turbulence analyses due to its clear physical interpretation and consistency with flow within the airspace, following (1, 4, 5).

A2.1 Mixing-Length Formulations. The turbulent momentum flux (TMF) is commonly modeled using a first-order closure:

$$\langle u'w' \rangle = -K_m \frac{\partial \langle u \rangle}{\partial z}, \quad \text{with} \quad K_m = \ell^2 \left| \frac{\partial \langle u \rangle}{\partial z} \right| \quad [A8]$$

Solving for ℓ, we obtain the following formulations:

Intrinsic Averaging.

$$\ell_I = \sqrt{\left| \frac{\langle u'w' \rangle_I}{\frac{\partial \langle u \rangle_I}{\partial z} + \langle u \rangle_I \frac{\partial \epsilon}{\partial z}} \right|} \quad [A9]$$

Comprehensive Averaging.

$$\ell_C = \sqrt{\left| \frac{\langle u'w' \rangle_C}{\epsilon \cdot \frac{\partial \langle u \rangle_C}{\partial z}} \right|} \quad [A10]$$

A3. Turbulence mixing length closure

Mixing length prediction against LES results. Figure S1 presents vertical profiles of the normalized mixing length (ℓ/H) derived from high-resolution large-eddy simulations (LES) for four urban canopies with varying plan area densities ($\lambda_p = 0.11$, 0.16, 0.25, 0.44). These LES results (open circles) serve as the reference dataset for evaluating the performance of the present model (solid lines) and the Building Effect Parameterization (BEP) by Santiago and Martilli (2010) (dashed gray lines). The rightmost panel shows the theoretical limiting cases at $\lambda_p = 0$ and $\lambda_p = 1$, consistent with classical free-shear and fully obstructed-layer turbulence assumptions, respectively.

The present model demonstrates close agreement with the LES data across all densities, accurately capturing both the magnitude and vertical distribution of ℓ/H. In contrast, the BEP formulation, while broadly consistent in trend, underpredicts mixing length magnitudes within the canopy layer and fails to represent the sharp transitions observed in the LES. The predictive fidelity of the new model is particularly evident near $z/H = 1$, where momentum exchange between canopy and overlying flow is most pronounced.

These results form the empirical foundation for the turbulence closure diagnostics and model development summarized in Figure 2 of the main text. By explicitly resolving the ℓ/H structure across a range of λ_p using LES, we ensure the proposed formulation is rooted in high-fidelity data and applicable over the full range of realistic urban canopy conditions.

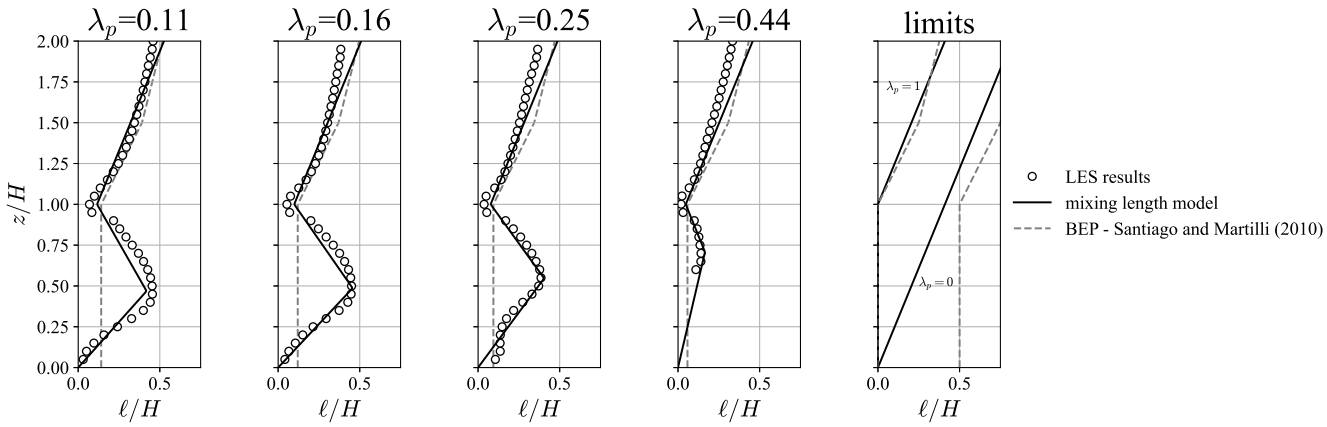

Fig. S1. Vertical profiles of normalized mixing length (ℓ/H) derived from large-eddy simulations (LES, circles), the present study's mixing length model (solid lines), and the Building Effect Parameterization (BEP) of Santiago and Martilli (2010) (dashed lines), for different plan area densities (λ_p). The rightmost panel illustrates theoretical limit cases ($\lambda_p = 0$ and $\lambda_p = 1$).

Comparison of mixing length predictions against realistic and real world LES results. To further evaluate the applicability of the proposed mixing-length formulation across realistic urban morphologies, we conducted comparisons against LES-derived profiles for both realistic Local Climate Zone (LCZ) classes (5) and real-world cities (7).

Figure S2 presents normalized vertical profiles of mixing length (ℓ/h_{mean}) for 12 LCZ categories simulated in Nagel et al. (2023) (5), capturing the breadth of global urban morphologies, from compact highrise (LCZ1) to sparsely built (LCZ9) and heavy industry (LCZ10). The present model (solid black lines) is benchmarked against the BEP formulation of Santiago and Martilli (2010) (dotted gray lines) and LES-derived profiles (dashed blue lines). Insets report the key morphological descriptors for each class, including plan area index (λ_p), frontal area index (λ_f), average and extreme building heights (h_{mean}, h_{min}, h_{max}), and height variability (σ_H), with 3D representations of the building layouts. Across all typologies, the present model achieves stronger agreement with LES than the BEP scheme, accurately reproducing peak values and vertical structure of ℓ in both dense and open configurations. This suggests that the closure is not limited to canonical canopies but is robust to diverse urban form factors.

Figure S3 extends the analysis to nine real-world urban sites across North America, Europe, and Australia. Using LES results from the UrbanTALES database (Nazarian et al., 2025) (7), we compare the present model and BEP parameterization against ℓ/h_{mean} profiles computed from fully resolved building-resolving LES. Despite variability in height distribution, layout regularity, and plan density across these cities, the present model consistently outperforms the Santiago and Martilli scheme. In particular, it reproduces the vertical extent and peak mixing values across complex layouts such as Manhattan and Paris, which include strong height gradients and nonuniform building arrangements. This supports the generalizability of the proposed formulation to operational applications involving realistic city geometries.

A4. Materials and methods: modeling tools

Large Eddy Simulation using `NekRS`. Using Large Eddy Simulation we expanded our data set via 3D simulations of canonical urban canopy flows using the high-order spectral element method (SEM) based computational fluid dynamics code `NekRS` (8). The computational domain was $L_z = 8H$ tall while in the streamwise and spanwise dimensions $L_x \times L_y$ the size of the domain was varied between $L_x = 18H$ and $30H$ for $\lambda_p = 0.11$ and 0.44 respectively, The spanwise direction was $L_y = 12$ for most of the cases except $\lambda_p = 0.16$ where the spanwise dimension of the domain was $L_y = 12.5$. The resolution of the SEM elements grid was 0.25H for the cases with $\lambda_p \leq 0.25$ ($\lambda_p = 0.11, 0.16, 0.25$), which combined with the order 7th which corresponds to 8 Gauss-Lobatto-Legendre points gives a resolution of $(0.25/8)H = 0.03125H$ (32 points per H). For the case of $\lambda_p = 0.44$, the element size was reduced to $0.125H$ and the polynomial order used was 5th order which corresponds to 6 Gauss-Lobatto-Legendre points gives a resolution of $(0.125/6)H = 0.0208H$ (48 points per H). It is important to stress that an additional E element was added near the ground and cuboid surface (see fig. S4). A full summary of all simulated cases and their associated morphological parameters is provided in Table S2.

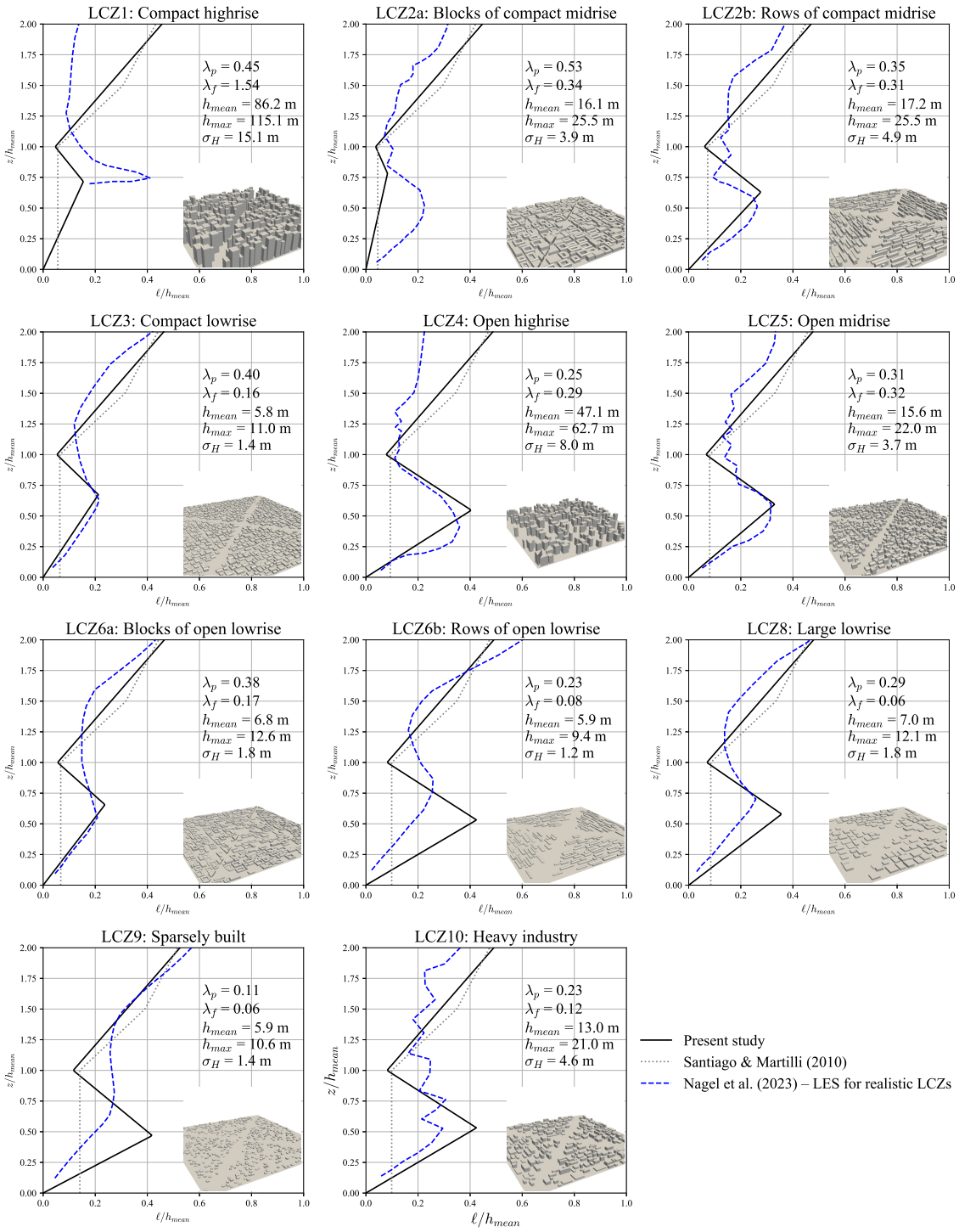

Fig. S2. Vertical profiles of normalized mixing length (ℓ/h_{mean}) for 12 realistic Local Climate Zone (LCZ) classes based on high-fidelity large-eddy simulations (LES) Nagel et al. (2023) (5). Each panel compares results from the present study's mixing length model (solid black lines) with the Building Effect Parameterization (BEP) of Santiago and Martilli (2010) (dotted gray lines) and LES-based profiles reported by Nagel et al. (2023) (dashed blue lines). Insets provide key morphological parameters: plan area index (λ_p), frontal area index (λ_f), mean height (h_{mean}), the minimum and maximum building heights (h_{min}, h_{max}) and the standard deviation of heights (σ_H). A 3D rendering of the corresponding building layout is shown in the lower-right corner of each panel. The profiles highlight the variability in mixing behavior across different urban typologies and demonstrate the improved agreement of the present model with LES data over conventional parameterizations.

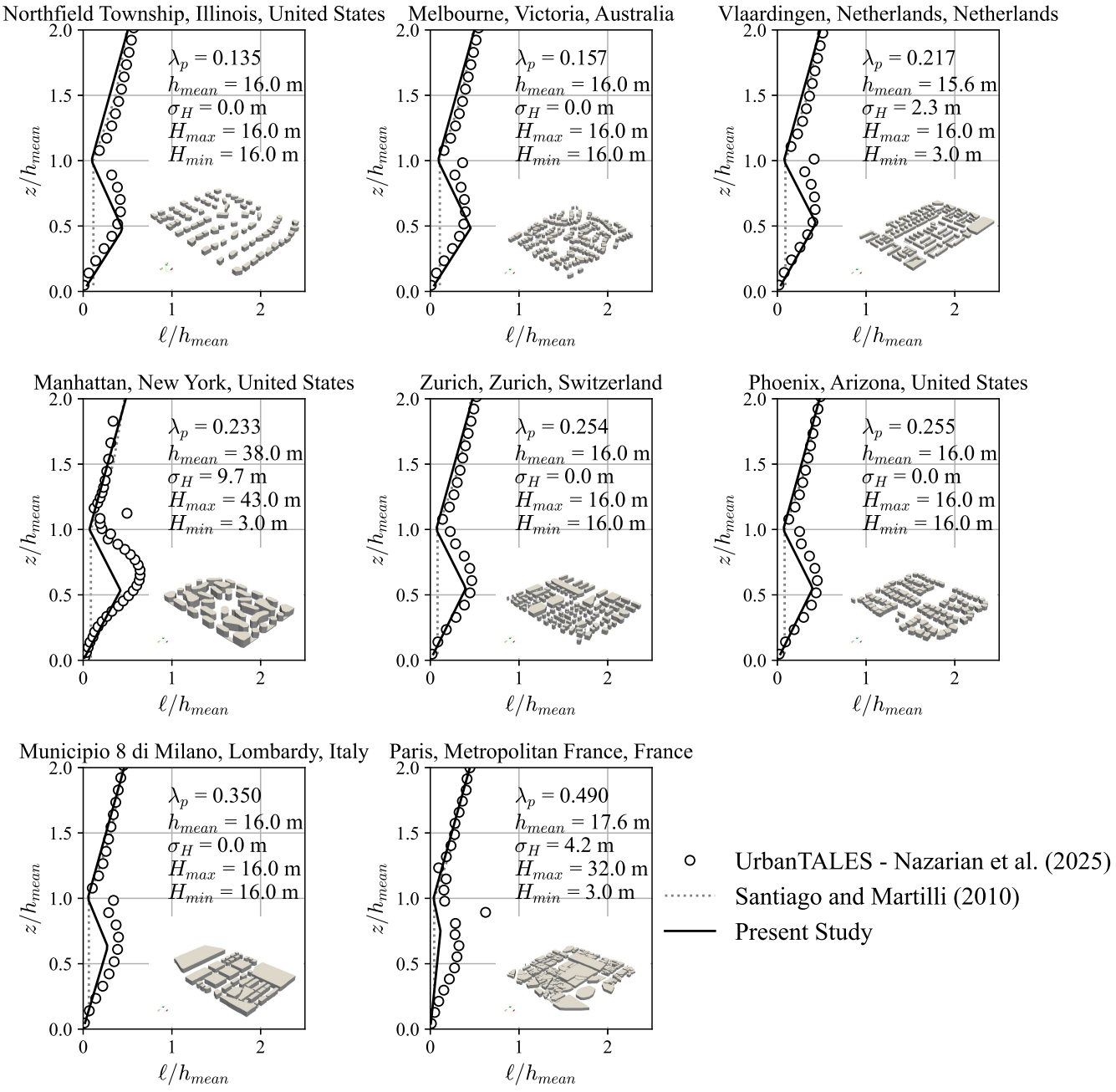

Fig. S3. Vertical profiles of normalized mixing length (ℓ/h_{mean}) for selected real-world urban morphologies across the United States, Europe, and Australia. Each panel shows comparisons between LES results from UrbanTALES by Nazarian et al. (2025) (open circles) (7), the present study's mixing length model (solid black lines), and the Building Effect Parameterization (BEP) of Santiago and Martilli (2010) (dotted gray lines). Urban domains span a range of plan area densities (λ_p), mean and maximum building heights (h_{mean}, H_{max}), and the heights standard (σ_H). Each panel includes a 3D rendering in the lower-right corner, illustrating the associated building arrangement. The results demonstrate that the present model better captures both the shape and magnitude of the mixing length profiles across diverse urban layouts, outperforming conventional parameterizations especially in cases with height variability and non-uniform building spacing.

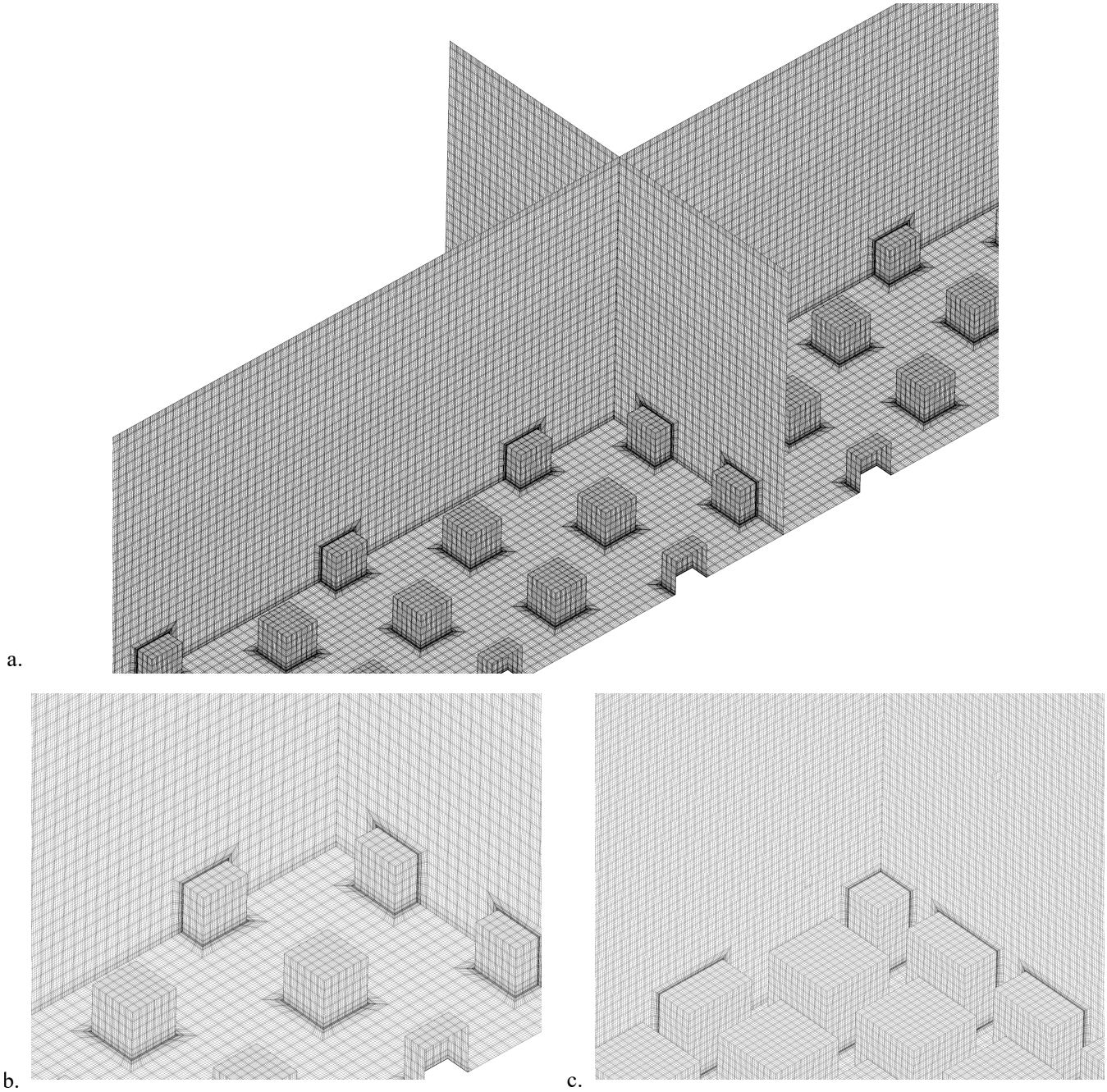

Fig. S4. Computational grid used for the numerical simulations of urban canopy flows, showing (a) an overview of the grid arrangement ($\lambda_p = 0.11$), (b) a detailed view near building corners ($\lambda_p = 0.11$), and (c) a close-up view of the refined grid resolution near building surfaces ($\lambda_p = 0.44$).

Table S2. Geometric and flow parameters for present LES and reference urban canopy simulations used for comparative analysis and mixing length model development.

Present study – LES									
Dataset	$\lambda_p - S/A$	$(L_x \times L_y \times L_z)/H$	N_x	N_y	npoints	$\mathrm{Re}_\infty = \frac{u_\infty H}{\nu}$	$\mathrm{Re}_H = \frac{u_H H}{\nu}$	$\mathrm{Re}_\tau = \frac{u_* H}{\nu}$	$\mathrm{Re}_b = \frac{u_b H}{\nu}$
Present study	$0.11 - S$	$30 \times 12 \times 8$	10	4	98,058,240	7,589	2,683	723.4	6,000
	$0.16 - S$	$25 \times 12.5 \times 8$	10	5	87,654,400	7,336	2,286	736.0	6,000
	$0.25 - S$	$20 \times 12 \times 8$	10	6	70,901,760	6,854	1,891	616.0	6,000
	$0.44 - S$	$18 \times 12 \times 8$	12	8	204,456,960	6,539	1,534	487.8	6,000
Literature studies									
Dataset	$\lambda_p - S/A$	$(L_x \times L_y \times L_z)/H$	N_x	N_y	$\mathrm{Re}_\infty = \frac{u_\infty H}{\nu}$				
Nazarian et al. (2020) (3)	$0.065 - S$	$24 \times 12 \times 7.4$	6	3	10^6				
	$0.11 - S$	$18 \times 9 \times 7.4$	6	3	10^6				
	$0.16 - S$	$15 \times 7.5 \times 7.4$	6	3	10^6				
	$0.25 - S$	$12 \times 6 \times 7.4$	6	3	10^6				
	$0.44 - S$	$10 \times 5 \times 7.4$	6	3	10^6				
	$0.065 - A$	$20 \times 12 \times 7.4$	5	3	10^6				
	$0.44 - A$	$7.5 \times 4.5 \times 7.4$	5	3	10^6				
Castro et al. (2017) (9)	$0.33 - A$	$12 \times 9 \times 8$	6	3	6,500				
	$0.33 - A'$	$12 \times 12 \times 12$	6	4	7,500				
Branford et al. (2011) (10)	$0.25 - A$	$16 \times 16 \times 8$	8	8	4,750				
	$0.25 - A'$	$16 \times 16 \times 8$	8	8	4,750				
Xie et al. (2008) (11)	$0.25 - S$	$16 \times 16 \times 10$	8	8	4,790				

***Xie et al. (2008) (11) performed simulations at $\lambda_p = 0.25$ using staggered cuboids with equal length and width but varying heights. Within each 4-by-4 unit, the building heights consisted of $1 \times 0.26H$, $3 \times 0.63H$, $7 \times 0.98H$, $4 \times 1.33H$, and $1 \times 1.68H$, where H is the average building height.**

The P_N–P_N spectral element formulation was adopted for all simulations (12). In this formulation, the velocity and pressure fields are both represented using tensor-product polynomials of degree p within each non-overlapping hexahedral element Ω_e, such that the global domain is $\Omega = \bigcup_{e=1}^{E} \Omega_e$. The basis functions are Lagrange interpolants defined on Gauss–Lobatto–Legendre (GLL) quadrature points, which ensures numerical stability and enables efficient pointwise quadrature operations within each element.

The incompressible filtered Navier–Stokes equations were solved using the GPU-accelerated spectral element solver `NekRS`, which provides exponential spatial convergence and second-order temporal accuracy. A de-aliasing procedure was applied to the nonlinear advection terms using the standard 3/2 over-integration rule (12). To balance spatial accuracy and computational performance, seventh-order elements $p = 7$ ($N = 8$ number of points per element) were used throughout. Time integration followed a mixed implicit–explicit scheme: all linear terms (e.g., viscous diffusion, pressure gradient) were treated implicitly using a projection method with pressure–velocity decoupling, while the nonlinear advection terms were treated explicitly. The time advancement used second-order backward differentiation (BDF2) for implicit terms and third-order extrapolation (EXT3) for explicit terms, consistent with a BDF2/EXT3 scheme. The LES was based on a spectral filtering approach, which act as an implicit high-pass filter for unresolved turbulent scales (13–15), thereby avoiding the need for an explicit subgrid-scale modeling using a transport equation.

Figure S5 presents a validation of the present study's large-eddy simulation (LES) results through a comparison of vertical profiles of mean velocity and Reynolds shear stress with previously published data. The panels show normalized mean velocity profiles ($\overline{u}/\overline{u}_H$ and $\overline{u}/u_*$) and Reynolds shear stress ($\overline{u'w'}/u_*^2$) across four different urban canopy densities ($\lambda_p = 0.11$, 0.16, 0.25, and 0.44). Simulation results from the present study are shown as lines, while symbols represent benchmark LES data from Nazarian et al. (2020) (7), enabling direct comparison across cases. The agreement between the two independent datasets confirms the fidelity of the current simulations in capturing both the velocity structure and momentum fluxes in and above the canopy. In particular, the present results match both the shape and magnitude of normalized velocity and stress profiles, reproducing key trends such as the shift of the velocity maximum with increasing λ_p and the inflection near the canopy top. Insets highlight the region inside the canopies.

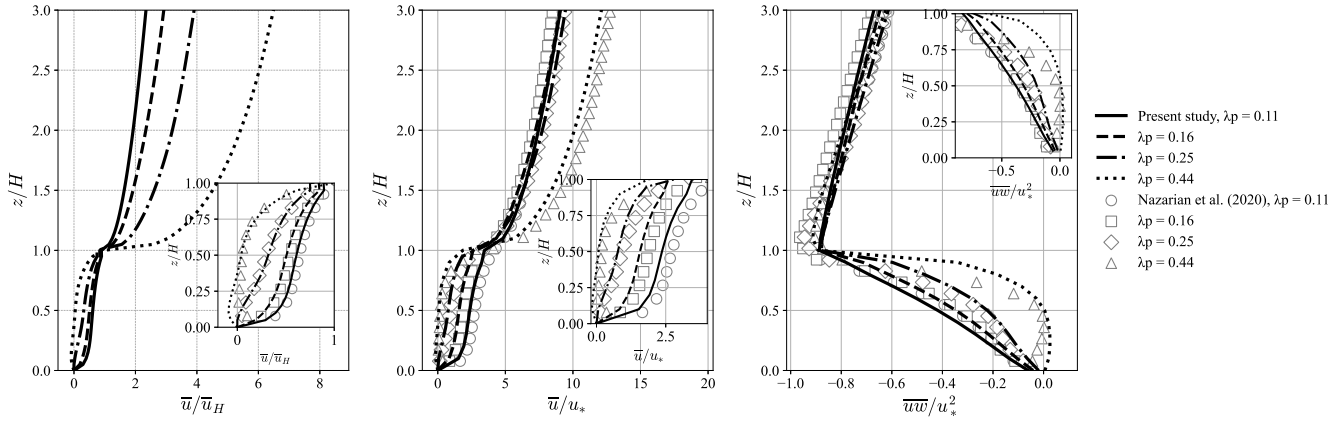

Fig. S5. Vertical profiles of normalized mean velocity ($\overline{u}/\overline{u}_H$ and $\overline{u}/u_*$) and Reynolds shear stress ($\overline{uw}/u_*^2$) for different plan area densities (λ_p), comparing the present study (lines) with numerical results from Nazarian et al. (2020) (symbols). Insets provide detailed views within the urban canopy.

Figure S6 presents one-dimensional turbulence spectra at multiple heights above urban canopies for a range of plan area densities (λ_p). Left panels show normalized velocity spectra $E(k_xH)/u_{2H}$ plotted against nondimensional wavenumber k_xH, with the characteristic $-5/3$ slope of the inertial subrange indicated with an orange line. Right panels show premultiplied spectra $k_xHE(k_xH)/u_b^2H$ as a function of normalized wavelength λ_x/H at selected vertical locations ($z/H = 1.05$, 1.2, 1.5, 2.0). The red dashed line marks the effective resolution limit, defined as twice the element size (2Δ).

The spectra confirm that all cases are well resolved in the inertial subrange. A clear $-5/3$ slope is observed across approximately one decade in k_xH, and the absence of energy accumulation near the resolution cutoff indicates low numerical dissipation and accurate capture of turbulent scales. Moreover, the energy content associated with scales smaller than the filter size is several orders of magnitude lower than that in the inertial range. The premultiplied spectra reveal changes in the distribution of turbulent energy with height. Near the canopy top ($z/H \approx 1.05$), energy is distributed more broadly across wavelengths due to strong wake-induced turbulence and multi-scale interactions. At higher elevations, the spectra become more sharply peaked. In all cases, the energy carried by scales near the filter size remains negligible, further confirming that the simulations are well resolved.

WRF Model Setup and Experiment Design. In this study, we used version 4.5.1 of the Weather Research and Forecasting (WRF) model (16), a non-hydrostatic, fully compressible numerical weather prediction system. To represent urban processes, we incorporated the Building Effect Parameterization (BEP) and the Building Energy Model (BEM) (17–19), which simulate urban canopy layer dynamics and associated building energy exchanges.

The simulations employed three two-way nested domains with horizontal grid spacings of 4.5 km, 1.5 km, and 500 m, respectively. The outer domain consisted of 404 × 403 grid points, the intermediate domain of 412 × 412 grid points, and the innermost domain—covering the Chicago Metropolitan Area (CMA)—also used 412 × 412 grid points (Figure S7a). The model integration time step was set to 15 seconds and was further adjusted for each domain based on Courant–Friedrichs–Lewy (CFL) conditions.

The vertical grid included 55 eta levels extending from the surface to approximately 20 km in altitude. To adequately capture lower atmospheric dynamics, enhanced vertical resolution was used near the surface, with 13 levels below 100 m and the first 5 layers located within 10 m above ground, each having a resolution of approximately 1–2 m. BEP-based models employ a secondary "urban grid" to resolve sub-grid urban morphology. For this study, we set the maximum number of vertical levels in the urban grid to 30, the vertical resolution of the urban grid to 3.0 m, and the maximum number of building types per urban class to 20.

Initial and boundary conditions were obtained from the fifth-generation ECMWF Reanalysis (ERA5) dataset (20), providing 3-hour updates at a spatial resolution of approximately 31 km. Simulations were initialized using ERA5 atmospheric fields, with land surface and soil variables interpolated to the WRF grid. To improve model accuracy over the Great Lakes region, ERA5 sea surface temperature (SST) fields were replaced with higher-resolution observations from the NOAA Great Lakes Surface Environmental Analysis (GLSEA) product (21), which provides daily maps at 1.3 km resolution. This substitution has been shown to enhance WRF performance in simulating near-surface air temperature and relative humidity over the Great Lakes (22).

The physics suite included the Noah land surface model (23), the Bougeault-Lacarrère planetary boundary layer (PBL) scheme (24), WRF Single-Moment 6-class microphysics (25), the Dudhia shortwave radiation scheme (26), and the Rapid Radiative Transfer Model (RRTM) for longwave radiation (27). WRF Preprocessing System (WPS) tools 4.6.0 were used for initial and boundary condition preparation. The simulations were initialized at 18 UTC on July 21, 2024, and ran until 00 UTC on July 24, 2024. The first 6 hours were discarded to allow for model spin-up. Model outputs were archived at hourly intervals. Urban geometry was characterized using Local Climate Zones (LCZs) derived from the World Urban Database and Access Portal Tool (WUDAPT) (28), and enhanced with high-resolution data from the Height Mapping of Trees and Buildings

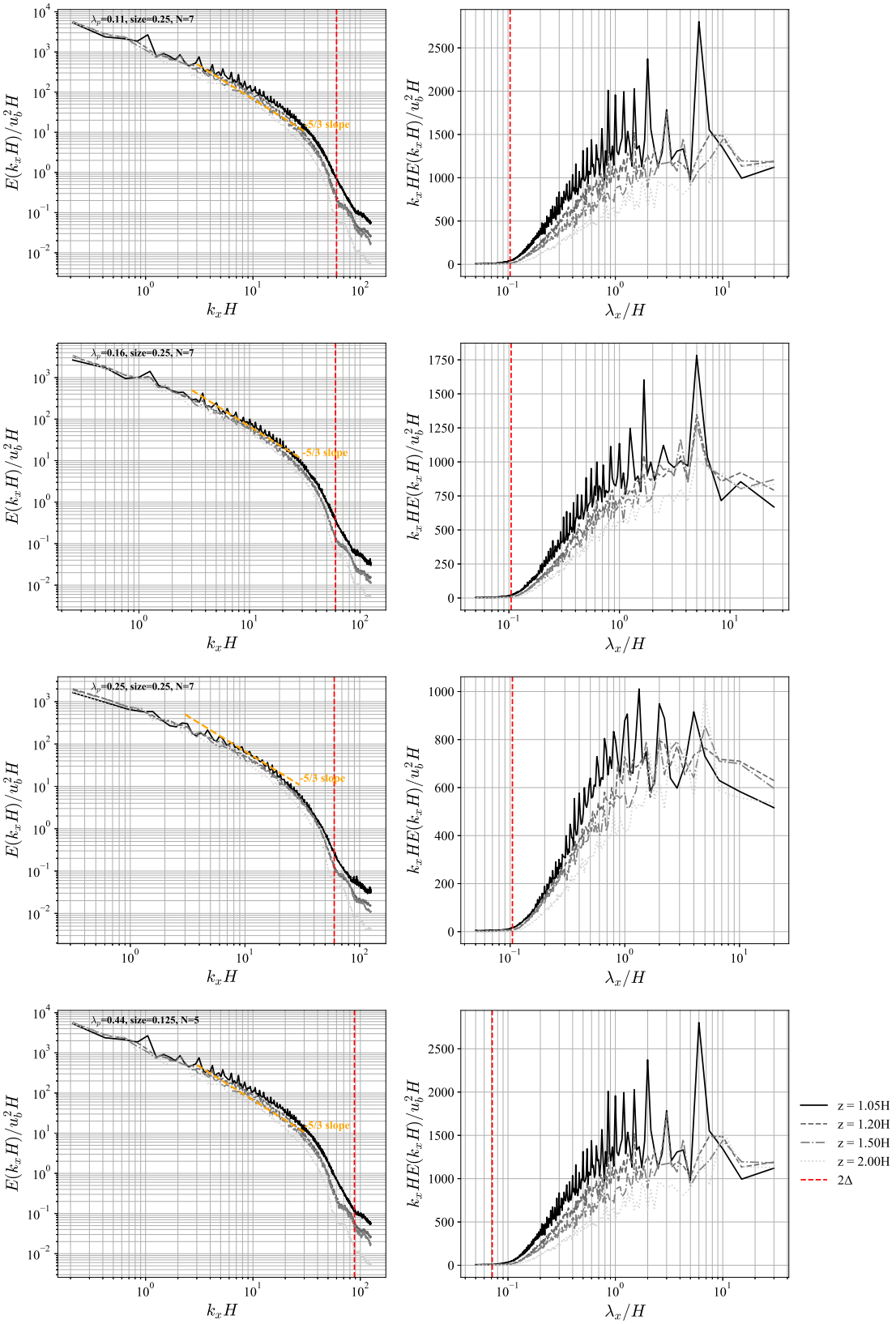

Fig. S6. One-dimensional turbulence spectra at various heights above urban canopies with different plan area densities (λ_p). Left panels show normalized spectra $E(k_xH)/u_b^2H$ plotted against wavenumber k_xH, with the characteristic $-5/3$ inertial subrange slope indicated. Right panels display premultiplied spectra $k_xHE(k_xH)/u_b^2H$ versus normalized wavelength λ_x/H at different vertical locations (z/H). The red dashed vertical line indicates twice the grid spacing (2Δ), marking the limit of spatial resolution.

(HiTAB) dataset (29). Within the Chicago Metropolitan Area (CMA), the urban geometry was further refined using the University of Texas – Global Building Heights for Urban Studies (UT-GLOBUS) dataset (30). Eleven distinct LCZ classes were defined based on prior studies and spatial datasets (31). Albedo and emissivity distributions over the Chicago area were refined using high-resolution data from Cheng et al. (32). Figure S7b shows the spatial distribution of LCZs applied over domain 3 (at a 500m resolution), with the red box in Figure S7a indicating the extent shown in Figure S7b.

To evaluate the robustness and added value of the proposed turbulence model, we conducted four comparative simulations over the CMA, varying both the urban morphology dataset and the turbulence parameterization. This design allows us to disentangle the respective influences of improved turbulence representation and enhanced urban morphology on model performance. The two levels of morphological detail—WUDAPT-based LCZs and the high-resolution HiTAB dataset—were each paired with both the original Santiago and Martilli (2010) scheme (1) and the new model proposed in this study. This setup enables a side-by-side evaluation of model skill across combinations of physical parameterizations and morphology resolutions, highlighting their respective roles in capturing spatial heterogeneity in urban microclimate conditions.

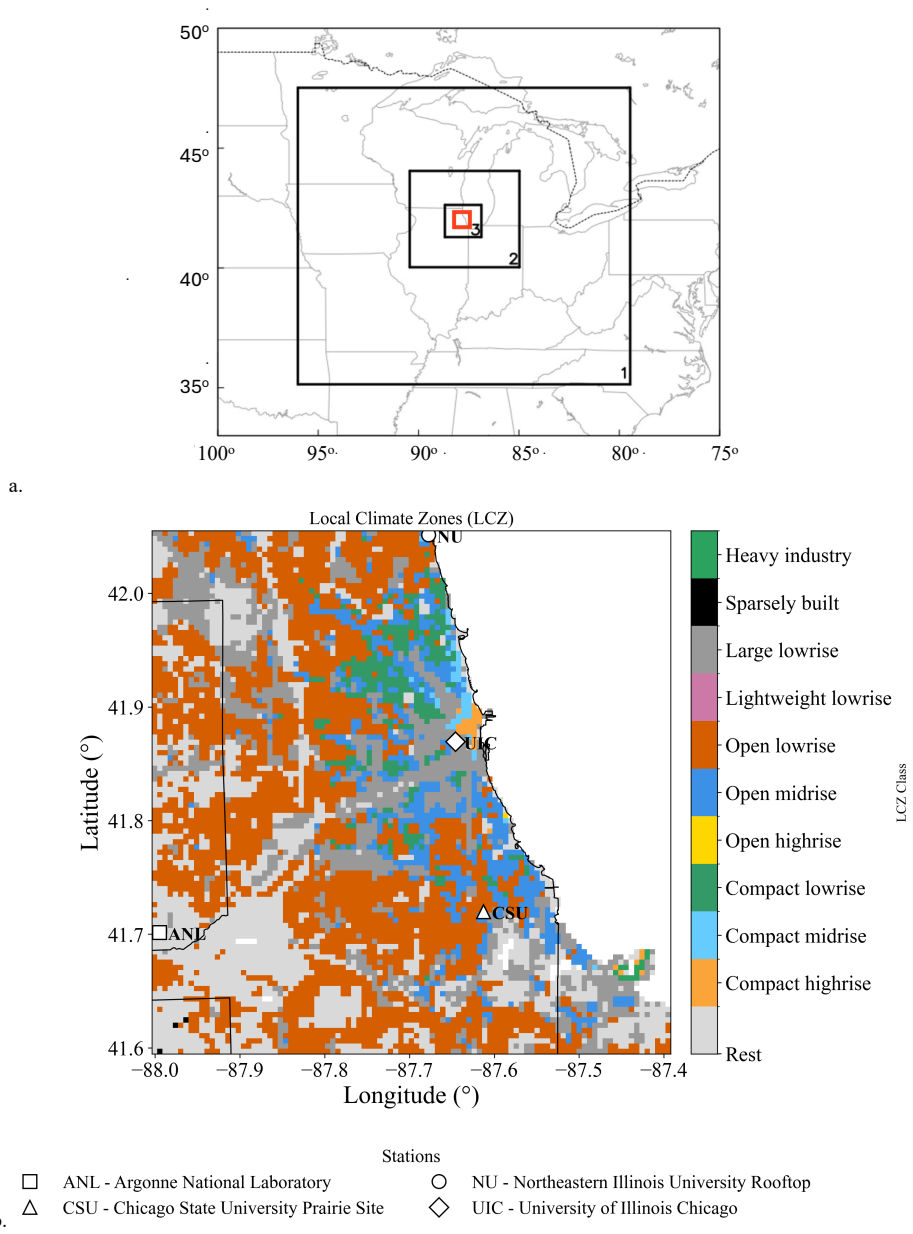

Fig. S7. (a) WRF domain. The red box indicates the Chicago Metropolitan Area (CMA). (b) The urban land-use categories after incorporating local climate zones (LCZs) from WUDAPT data over domain 3.

A5. WRF data analysis

Model validation. To evaluate model performance against in-situ observations, we selected four urban monitoring sites within the Chicago Metropolitan Area, shown in Fig. S7b (33, 34). These sites span a range of urban contexts and LCZs, and include rooftop and near-surface installations. Table S3 summarizes their geographic coordinates and measurement heights above ground level. Each of these sites is equipped with a Vaisala Weather Transmitter (WXT530 series), which provides measurements of ambient temperature ($\pm 0.3^{\circ}$C accuracy), pressure (± 0.5 hPa at $0 \ldots +30^{\circ}$C accuracy), and relative humidity ($\pm 3\%$ RH at RH $< 90\%$ accuracy) via an RC oscillator and dual reference capacitors within the sensor PTU module.

Figures S8-S10 present time series comparisons of modeled and observed meteorological variables at the four urban monitoring sites at Argonne National Laboratory (ANL), Chicago State University (CSU), Northwestern University (NU), and University of Illinois Chicago (UIC) within the CMA. Each panel shows results for the present study and the Santiago and Martilli (2010) (1) scheme, using both WUDAPT and HiTAB urban morphology datasets, against observational data (open circles).

Table S3. Station metadata used for model–observation comparison.

Site ID	Latitude (°N)	Longitude (°W)	Height (m AGL)	Site Overview
ANL	41.7016	–87.9951	2.0	Open prairie surrounded by light forest, minimal urban influence
CSU	41.7200	–87.6128	2.0	College campus with scattered buildings and open green space
NU	42.0514	–87.6776	15.69	College rooftop with wide urban exposure near Lake Michigan
UIC	41.8694	–87.6459	2.0	College campus within the urban interior

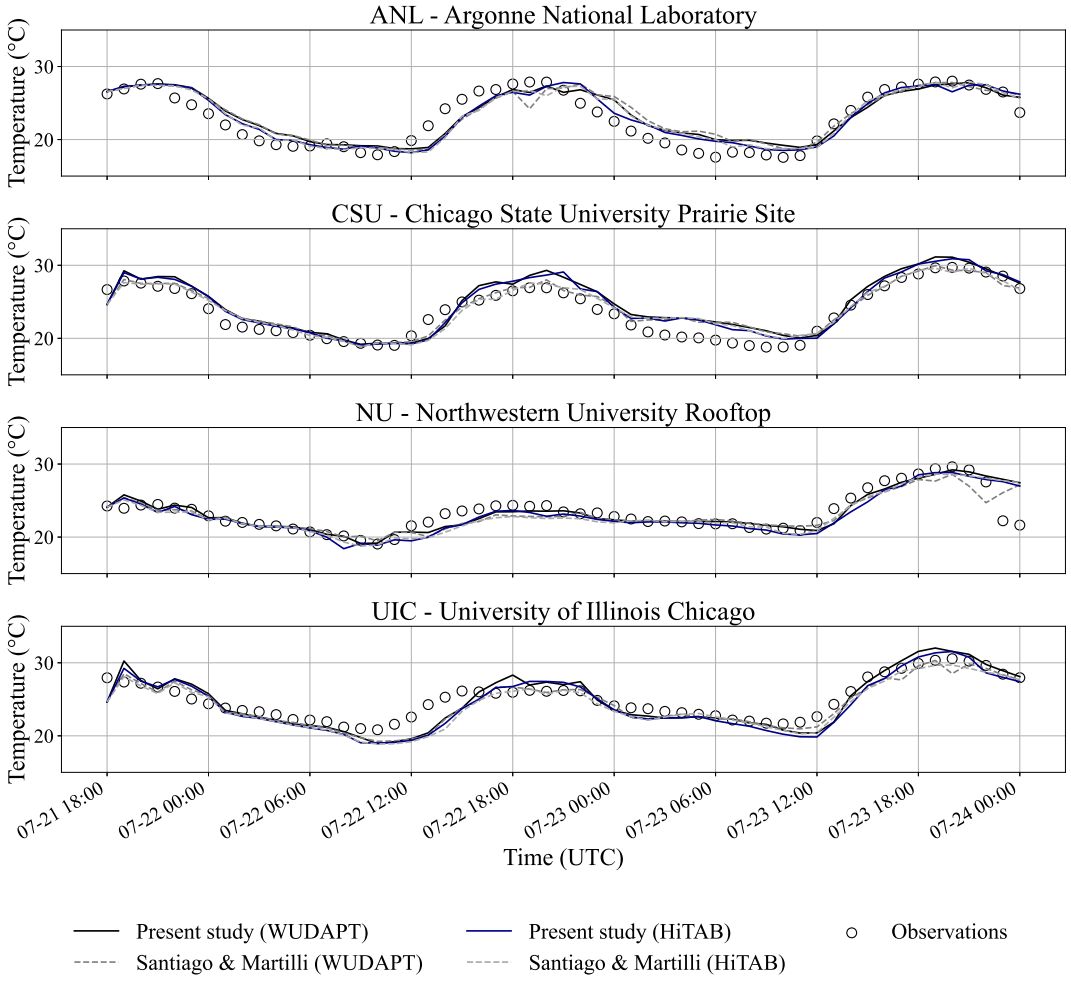

Fig. S8. Time series of observed and modeled temperature at four urban observation sites (ANL, CSU, NU, and UIC) from July 21 to July 24 2024.The present study's simulations using WUDAPT and HiTAB urban morphology datasets are shown with black and blue lines, respectively, and are compared to the Santiago and Martilli (2010) scheme (red and gray dashed lines). Observations are shown as open circles.

Figure S8 shows near-surface air temperature, revealing consistent diurnal patterns and generally good agreement between modeled and observed temperatures. The present study tends to better capture daytime peaks and nighttime minima, particularly at NU and UIC. Figure S9 displays near-surface relative humidity (RH), where the present model generally improves both the magnitude and timing of RH evolution, especially during day–night transitions. This improvement is most evident at ANL and CSU, with good agreement also observed at NU and UIC despite some overestimation during nighttime hours. Figure S10 shows wind speed comparisons, with larger variability and site-specific differences, though the present study captures temporal trends effectively. Further quantitative evaluation of these time series, including regression, RMSE, % error and observed-versus-modeled scatter plots, is provided in the main text (see Fig. 4), where we further assess the predictive performance of each configuration.

Relative Humidity and Cooling Energy Consumption . Figures S11 and S12 provide four experiment simulated statistical comparisons of RH and urban cooling energy consumption between the Present Study and the Santiago and Martilli (2010) scheme (S&M) across the CMA.

Figure S11 shows RH distributions from both models and datasets (panels a–b, e–f), along with spatial maps of ΔRH (Present − S&M; panels c, g) and associated probability density functions (panels d, h). The present model yields lower RH values in regions that exhibit higher temperatures (see Fig.4), consistent with increased turbulent mixing. While domain-averaged RH differences are modest (typically 1–6% for WUDAPT and 1–3% for HiTAB), the spatial coherence of Δ RH patterns reflects canopy-layer sensitivity to updated turbulence representations. Inter-dataset differences (HiTAB − WUDAPT; panels i–j) further reveal the role of urban morphology in modulating humidity. Violin plots (panels k–l) summarize the effect of turbulence modeling approaches on the full RH distributions and Δ RH across all cases. The present study generally shows higher RH values and distinct distribution shapes compared to S&M, with differences in spread and central tendency reflecting sensitivity to both canopy formulation and urban morphology dataset.

Figure S12 provides a similar comparison for building energy consumption. Panels a–b and e–f show total cooling energy use from the Present Study and S&M, while panels c and g display the spatial differences (Δ Energy = Present − S&M) along with corresponding probability density functions. Energy use is highly sensitive to both the urban canopy representation and the turbulence parameterization: the present model systematically predicts higher cooling demand, especially in denser areas where canopy-layer mixing is more strongly enhanced. Although the absolute values are larger in WUDAPT due to its greater total building volume (resulting from a higher number of floors), the overall patterns and inter-model differences remain consistent across both morphology datasets. Inter-dataset contrasts (panels i–j) and violin plots (panels k–l) further reinforce these findings, with the Present Study showing higher mean, median, and maximum energy values, and broader distribution tails relative to S&M.

LCZ-Resolved temperature, RH, and Cooling energy distributions. Figures S13–S18 present LCZ-resolved probability distributions of air temperature, RH, and cooling energy consumption across Cook County, Illinois, using both WUDAPT and HiTAB urban morphology datasets. These distributions provide a detailed evaluation of model behavior within distinct urban typologies and complement the domain-wide analyses discussed in the main text.

Figures S13 and S14 show average temperature distributions per LCZ for the WUDAPT and HiTAB experiments, respectively. In both datasets, the Present Study predicts higher mean temperatures than the Santiago and Martilli (2010) scheme in mid-density LCZs, particularly compact lowrise (LCZ3), compact midrise (LCZ2), open midrise (LCZ5), and open lowrise (LCZ6). These zones, characterized by active within-canopy turbulence, exhibit clear rightward shifts in the Present Study's PDFs and heavier right tails in the ΔT distributions. Differences reach up to 2.4°C in WUDAPT and 1.5°C in HiTAB, highlighting the role of enhanced mixing in amplifying thermal exposure. In contrast, LCZs with sparse or industrial configurations (e.g., LCZs 9, 10, and "Rest") show minimal changes, as expected due to weak or inactive canopy-layer parameterizations.

Figures S15 and S16 display average RH2 distributions per LCZ modeled by experiments using WUDAPT and HiTAB, respectively. The present model consistently predicts reduced RH2 in zones that also exhibit stronger warming. Compact and open midrise/lowrise LCZs show RH2 reductions of 2–6% in WUDAPT and 1–3% in HiTAB, with negatively skewed Δ RH distributions reflecting localized drying. The observed RH reductions likely reflect increased turbulent transport and mixing-driven warming near the surface, consistent with the enhanced canopy-layer turbulence captured by the updated mixing-length model. Again, differences in RH are negligible in LCZs where building-induced turbulence is relatively weaker.

Figures S17 and S18 show the distribution of modeled average cooling energy demand per LCZ in the four experiments. In general, the present study yields significantly higher energy use than S&M in mid-density zones, with the strongest differences in compact and open lowrise categories (LCZs 3, 5, and 6). For WUDAPT (Fig. S17), mean per-cell ΔEnergy exceeds 2,000 kWh in these categories. In HiTAB (Fig. S18), absolute values are lower due to reduced building floor counts, but the relative patterns persist, with mean differences of 500–1,000 kWh. The "Rest" category (where energy consumption is zero) and LCZs with minimal built volume show no significant differences between models.

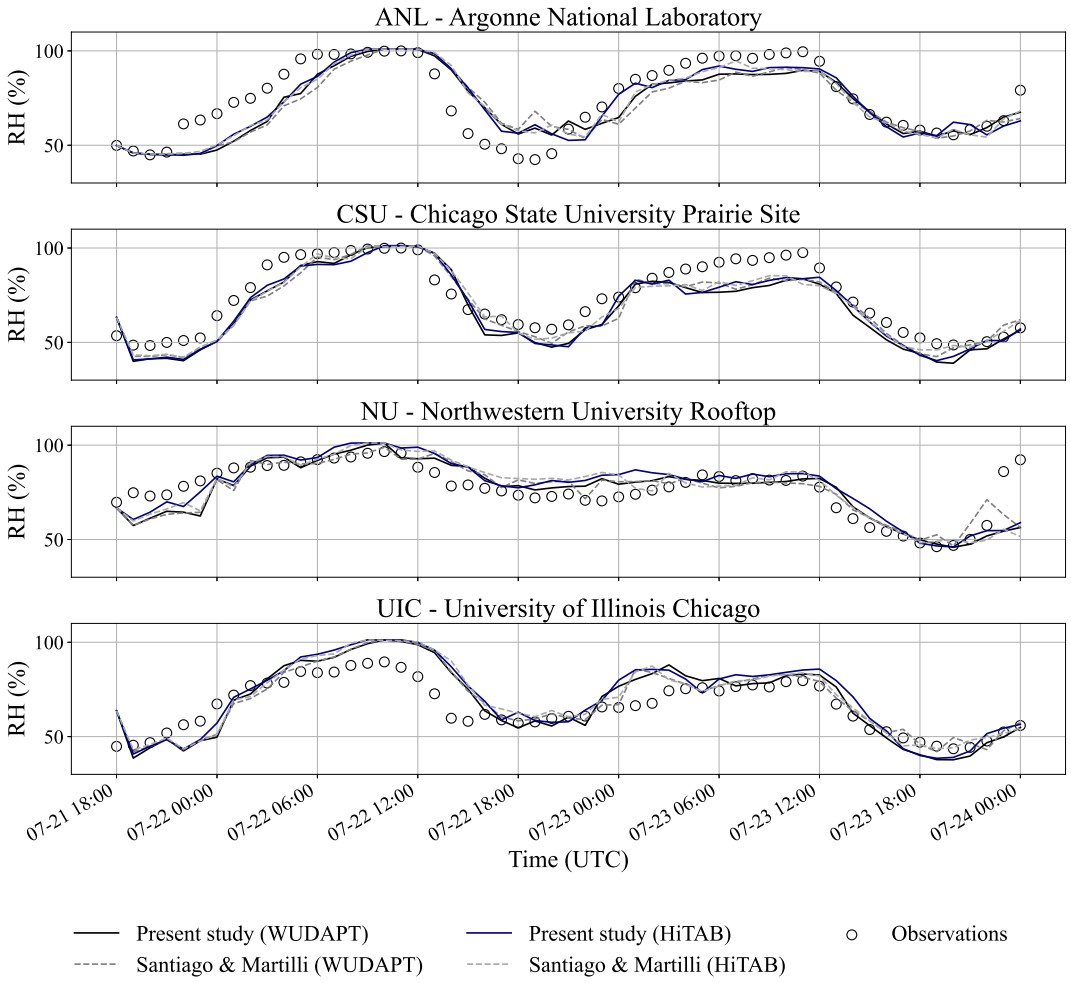

Fig. S9. Time series of observed and modeled near-surface air temperature at four urban observation sites (ANL, CSU, NU, and UIC) from July 21 to July 24, 2024. The present study's simulations using WUDAPT and HiTAB urban morphology datasets are shown with black and blue lines, respectively, and are compared to the Santiago and Martilli (2010) scheme (red and gray dashed lines). Observations are shown as open circles.

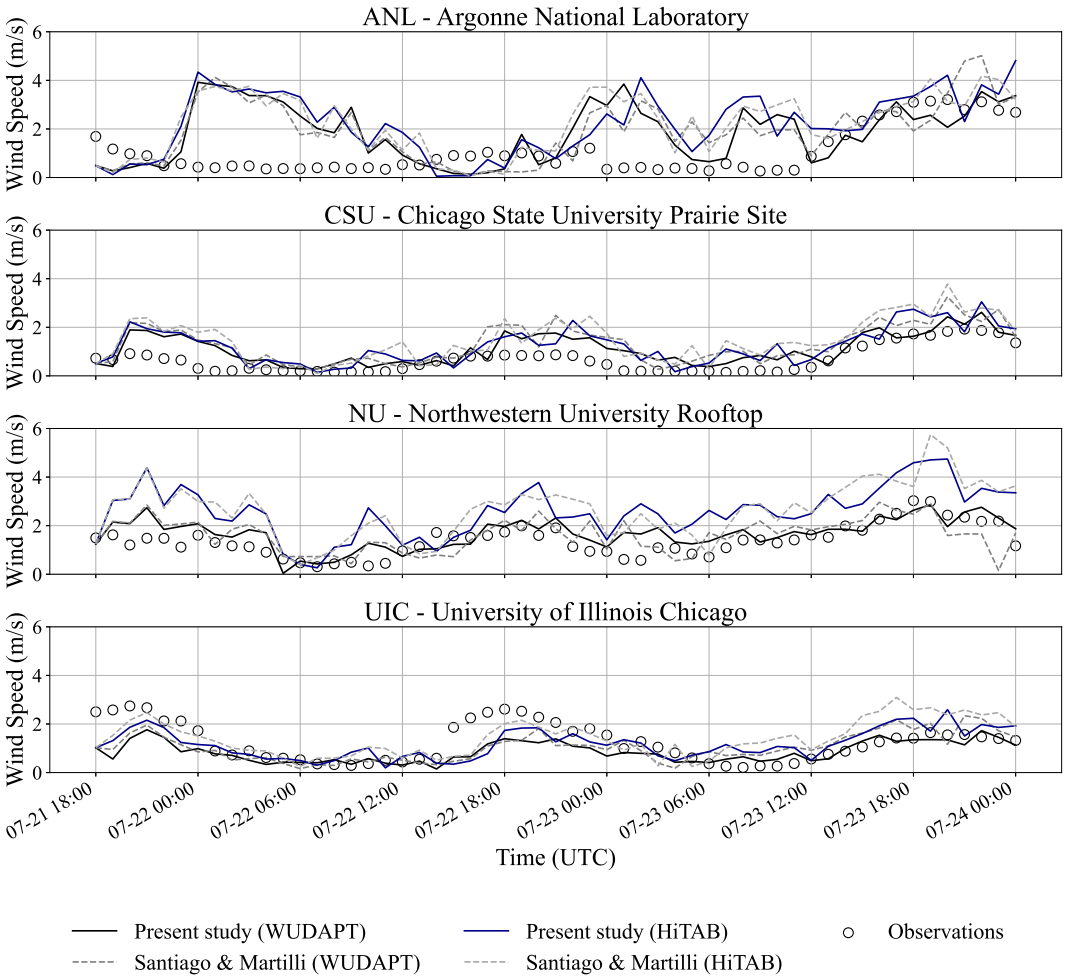

Fig. S10. Time series of observed and modeled wind speed at four urban observation sites (ANL, CSU, NU, and UIC) from July 21 18UTC to July 24 00UTC, 2024.The present study's simulations using WUDAPT and HiTAB urban morphology datasets are shown with black and blue lines, respectively, and are compared to the Santiago and Martilli (2010) scheme (red and gray dashed lines). Observations are shown as open circles.

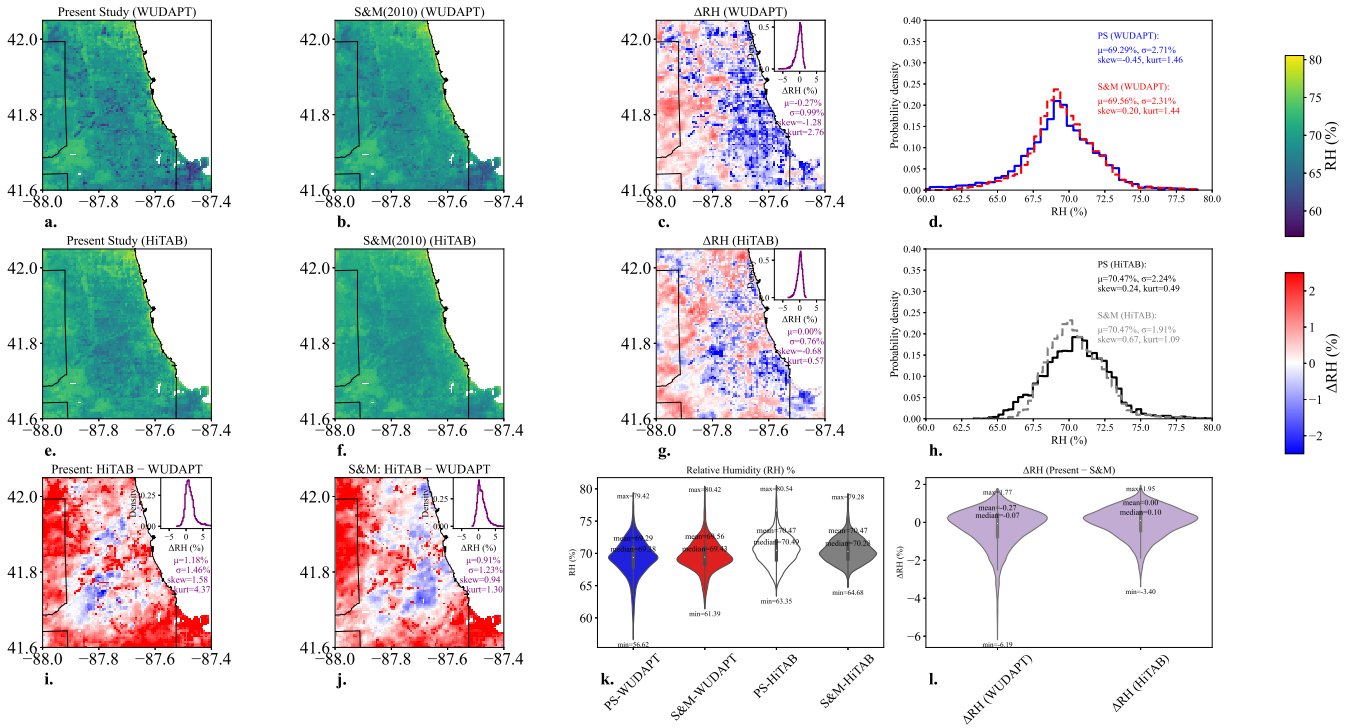

Fig. S11. Comparison of near-surface relative humidity (RH) from the Present Study and Santiago and Martilli 2010 (S&M) (1) using two urban morphology datasets: WUDAPT and HiTAB, over Cook County, Illinois. (a, b) Time-averaged RH fields from the Present Study and S&M using WUDAPT. (c) Spatial distribution of RH difference ΔRH (Present − S&M) for WUDAPT, with inset showing the PDF and summary statistics. (d) Probability density functions (PDFs) of RH comparing Present Study and S&M (WUDAPT). (e, f) Same as (a, b), but using the HiTAB dataset. (g) ΔRH (Present − S&M) for HiTAB, with inset PDF. (h) PDFs comparing Present Study and S&M using HiTAB. (i, j) Inter-dataset comparison of HiTAB − WUDAPT for Present Study and S&M, respectively, with inset PDFs and distribution metrics. (k) Violin plots of RH for all cases (Present and S&M, WUDAPT and HiTAB), showing distribution shape, mean, median, min, and max. (l) Violin plots of ΔRH distributions between Present Study and S&M using WUDAPT and HiTAB, annotated with statistical summaries. Colorbars indicate RH (%) and ΔRH (%).

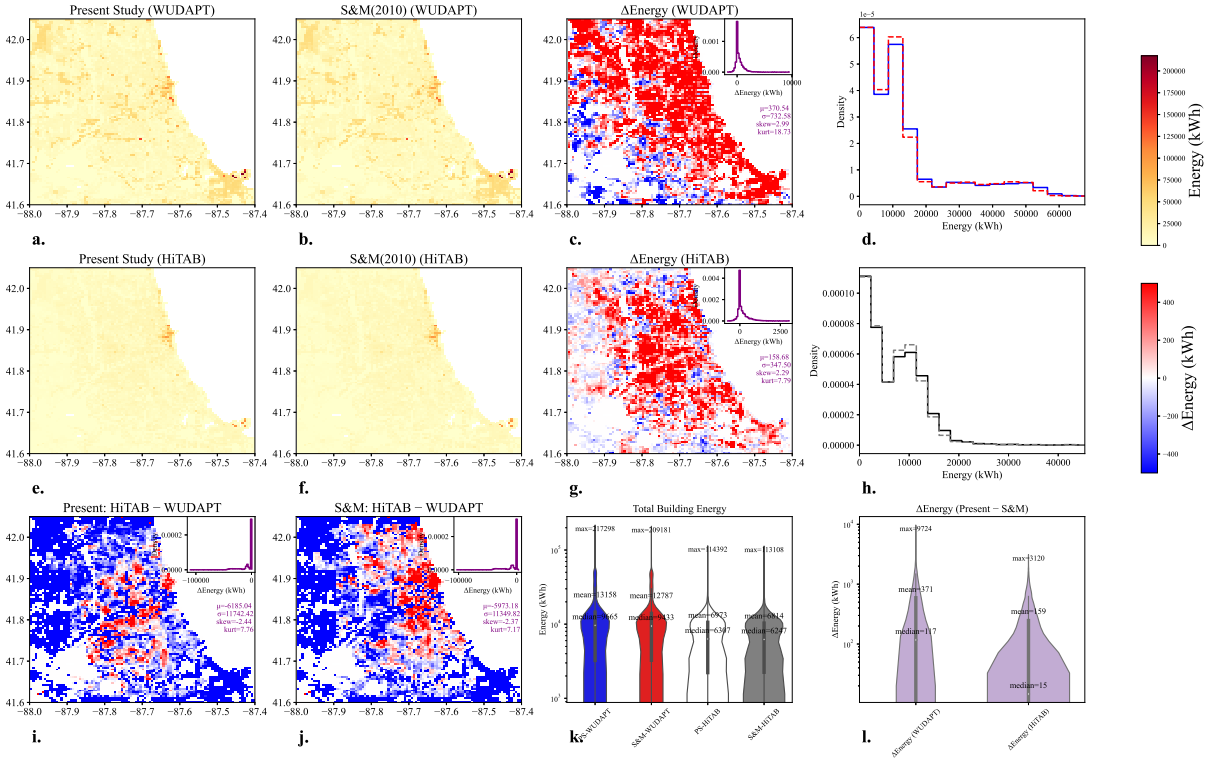

Fig. S12. Comparison of urban building energy consumption from the Present Study and Santiago and Martilli 2010 (S&M) (1) using two urban morphology datasets: WUDAPT and HiTAB, over Cook County, Illinois. (a, b) Total cooling energy use from the Present Study and SM using WUDAPT. (c) Spatial distribution of energy use difference ΔEnergy (Present − S&M) for WUDAPT, with inset showing the PDF and summary statistics. (d) Probability density functions (PDFs) of energy use comparing Present Study and S&M (WUDAPT). (e, f) Same as (a, b), but using the HiTAB dataset. (g) ΔEnergy (Present − S&M) for HiTAB, with inset PDF. (h) PDFs comparing Present Study and S&M using HiTAB. (i, j) Inter-dataset comparison of HiTAB − WUDAPT for Present Study and S&M, respectively, including inset PDFs and summary metrics. (k) Violin plots of total cooling energy use for all cases (Present and S&M, WUDAPT and HiTAB), showing distribution shape, mean, median, min, and max. (l) Violin plots of ΔEnergy distributions between Present Study and S&M using WUDAPT and HiTAB, annotated with statistical summaries. Colorbars indicate total energy and Δ Energy in kilowatt-hours (kWh).

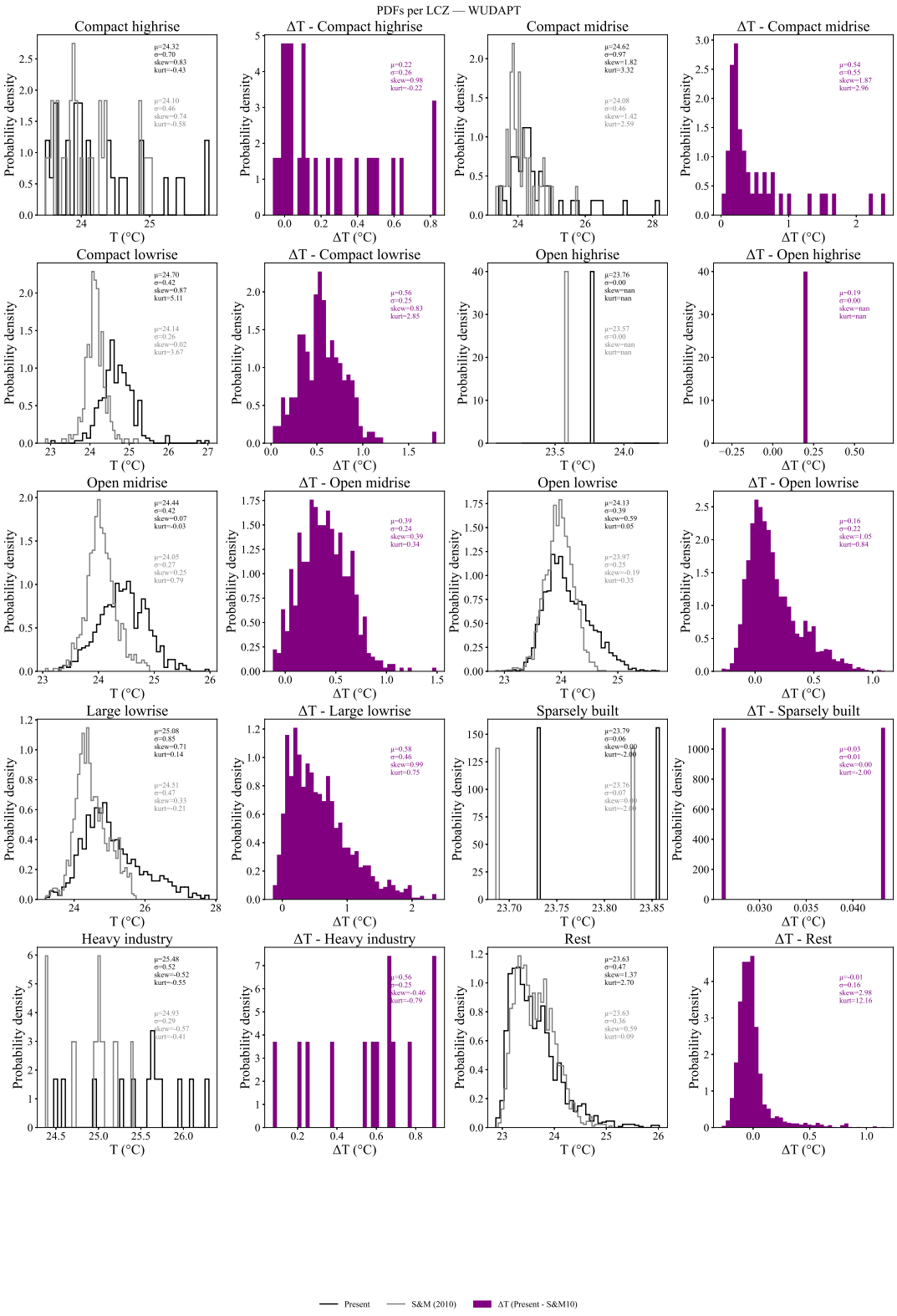

Fig. S13. Probability density functions (PDFs) of near-surface temperature (T) for different Local Climate Zones (LCZs), comparing the present study (black lines) and Santiago and Martilli (2010) (gray lines). Each row represents different LCZ categories. Middle panels show PDFs of the temperature differences (ΔT) between the two modeling approaches (present study minus Santiago and Martilli, 2010). Statistics displayed include mean (μ), standard deviation (σ), skewness (skew), and kurtosis (kurt).

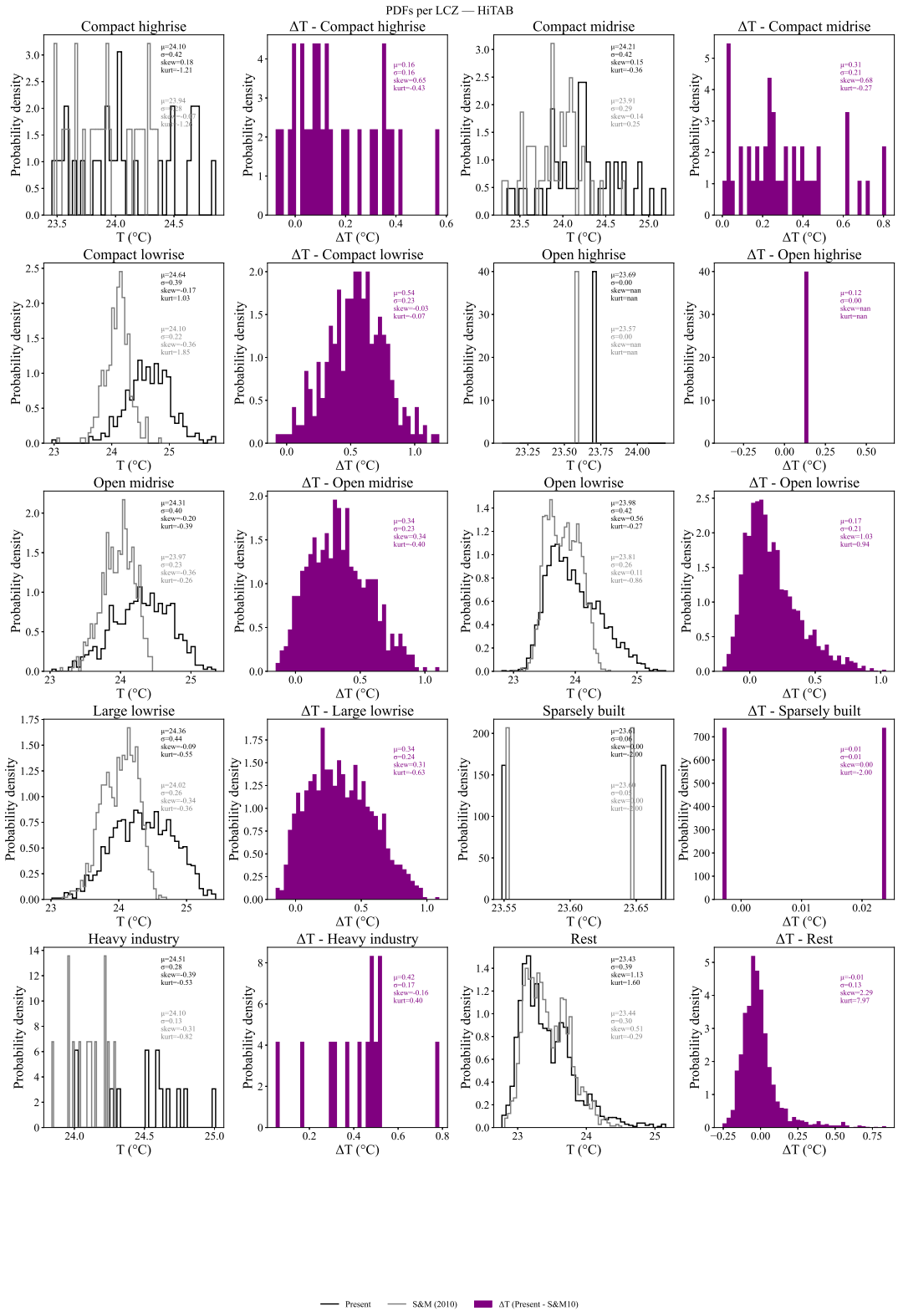

Fig. S14. Probability density functions (PDFs) of near-surface temperature (T) for different Local Climate Zones (LCZs), comparing the present study (black lines) and Santiago and Martilli (2010) (gray lines). Each row represents different LCZ categories. Middle panels show PDFs of the temperature differences (ΔT) between the two modeling approaches (present study minus Santiago and Martilli, 2010). Statistics displayed include mean (μ), standard deviation (σ), skewness (skew), and kurtosis (kurt).

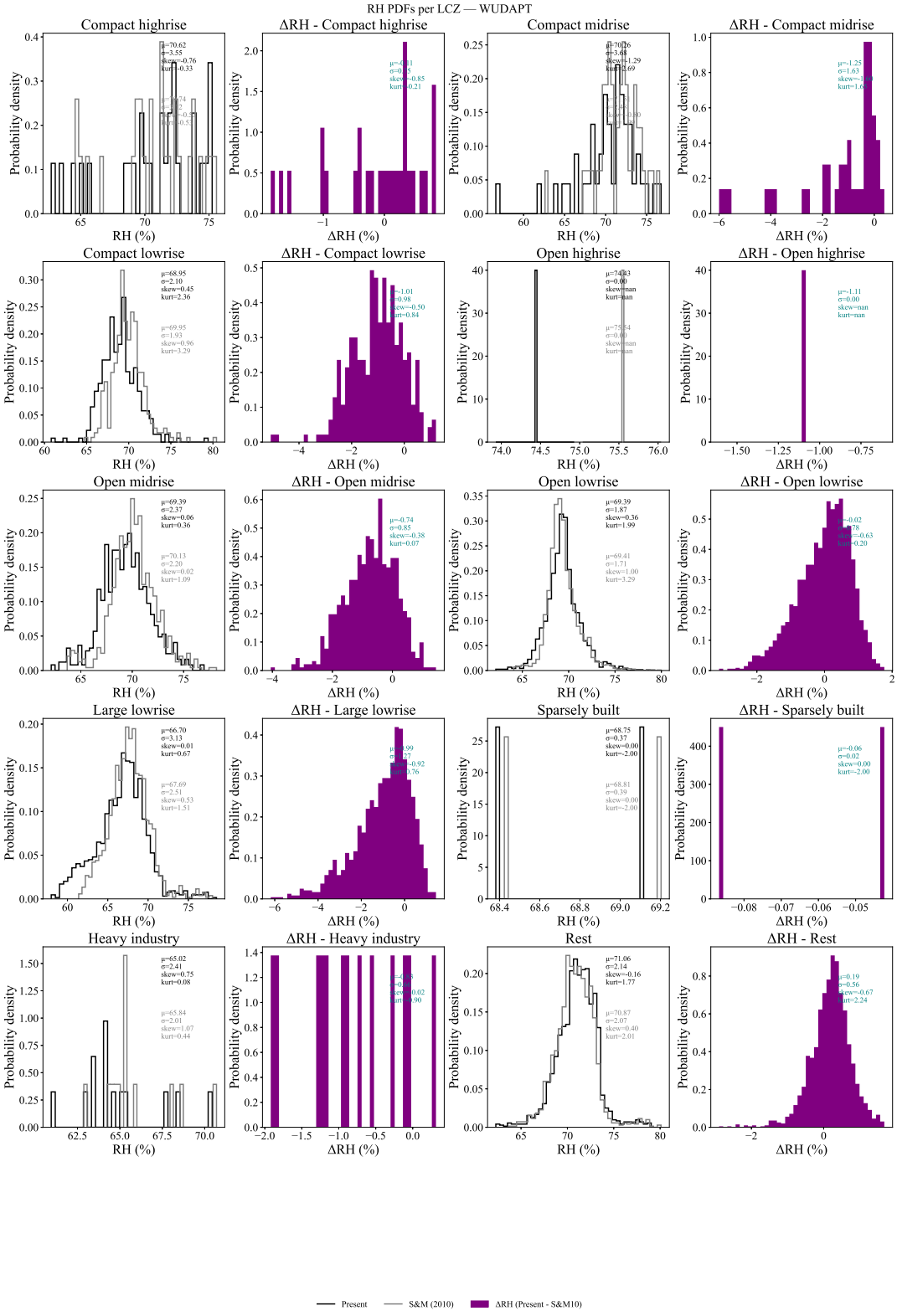

Fig. S15. Probability density functions (PDFs) of near-surface temperature (T) for different Local Climate Zones (LCZs), comparing the present study (black lines) and Santiago and Martilli (2010) (gray lines). Each row represents different LCZ categories. Middle panels show PDFs of the temperature differences (ΔT) between the two modeling approaches (present study minus Santiago and Martilli, 2010). Statistics displayed include mean (μ), standard deviation (σ), skewness (skew), and kurtosis (kurt).

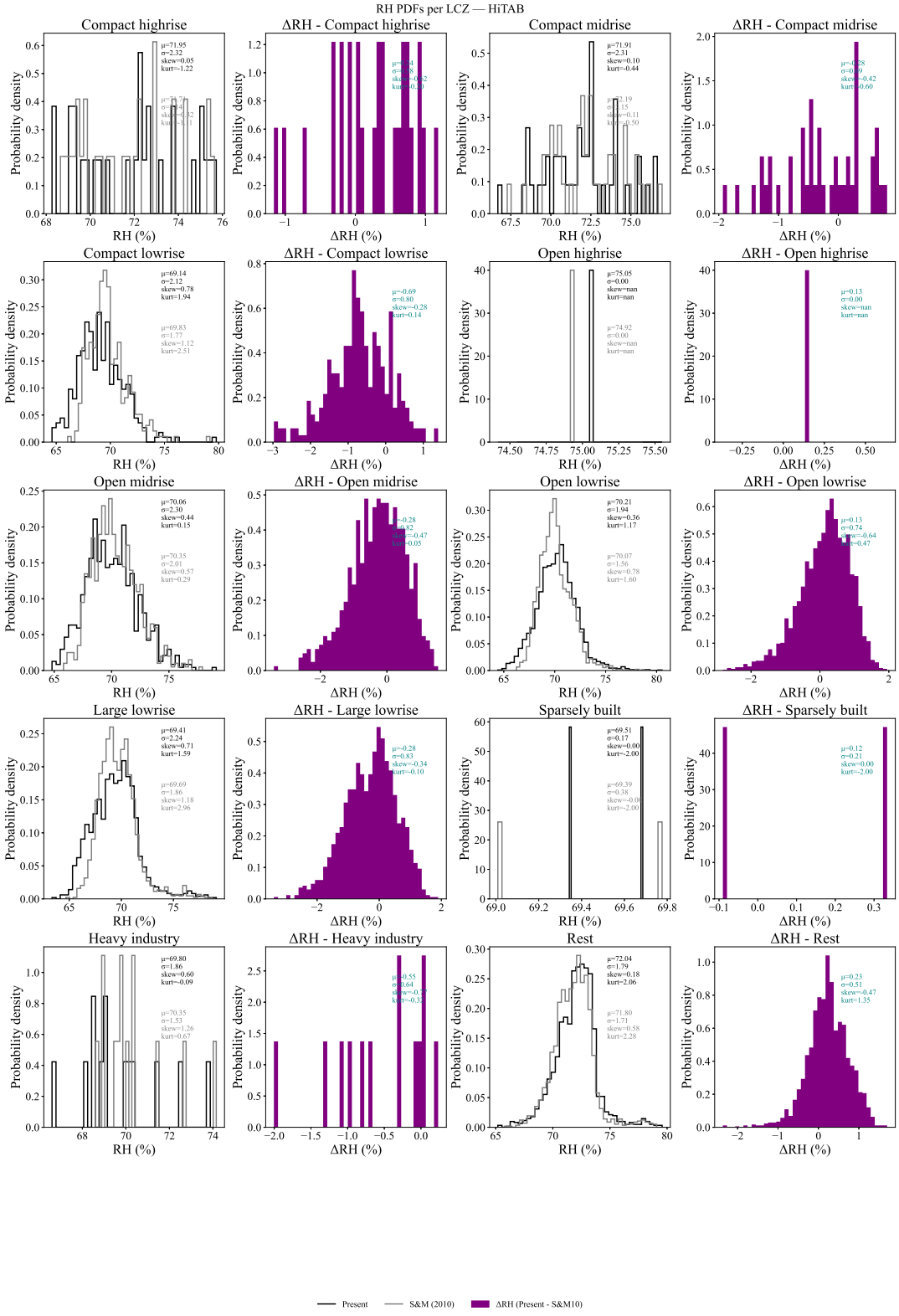

Fig. S16. Probability density functions (PDFs) of near-surface temperature (T) for different Local Climate Zones (LCZs), comparing the present study (black lines) and Santiago and Martilli (2010) (gray lines). Each row represents different LCZ categories. Middle panels show PDFs of the temperature differences (ΔT) between the two modeling approaches (present study minus Santiago and Martilli, 2010). Statistics displayed include mean (μ), standard deviation (σ), skewness (skew), and kurtosis (kurt).

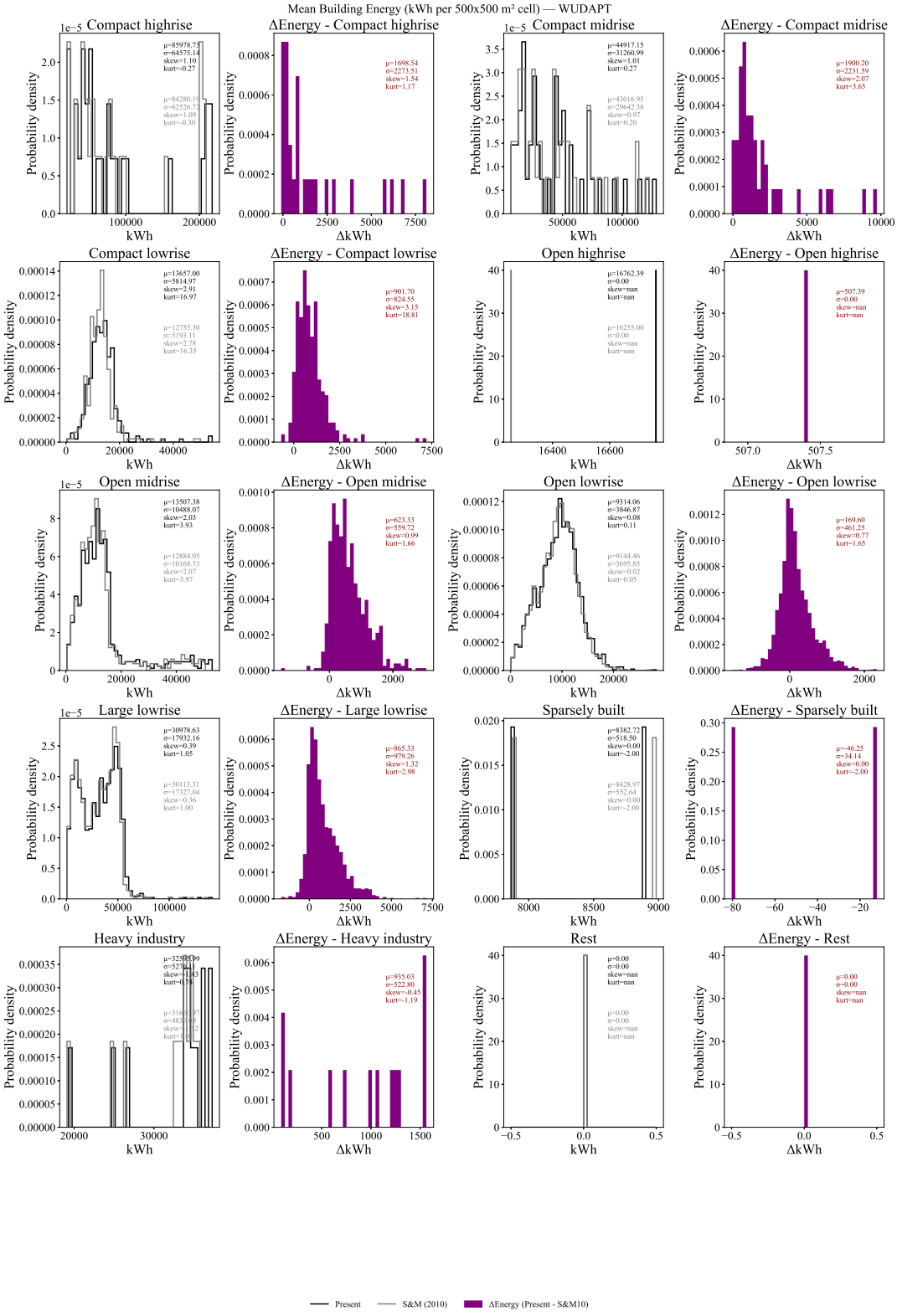

Fig. S17. Probability density functions (PDFs) of near-surface temperature (T) for different Local Climate Zones (LCZs), comparing the present study (black lines) and Santiago and Martilli (2010) (gray lines). Each row represents different LCZ categories. Middle panels show PDFs of the temperature differences (ΔT) between the two modeling approaches (present study minus Santiago and Martilli, 2010). Statistics displayed include mean (μ), standard deviation (σ), skewness (skew), and kurtosis (kurt).

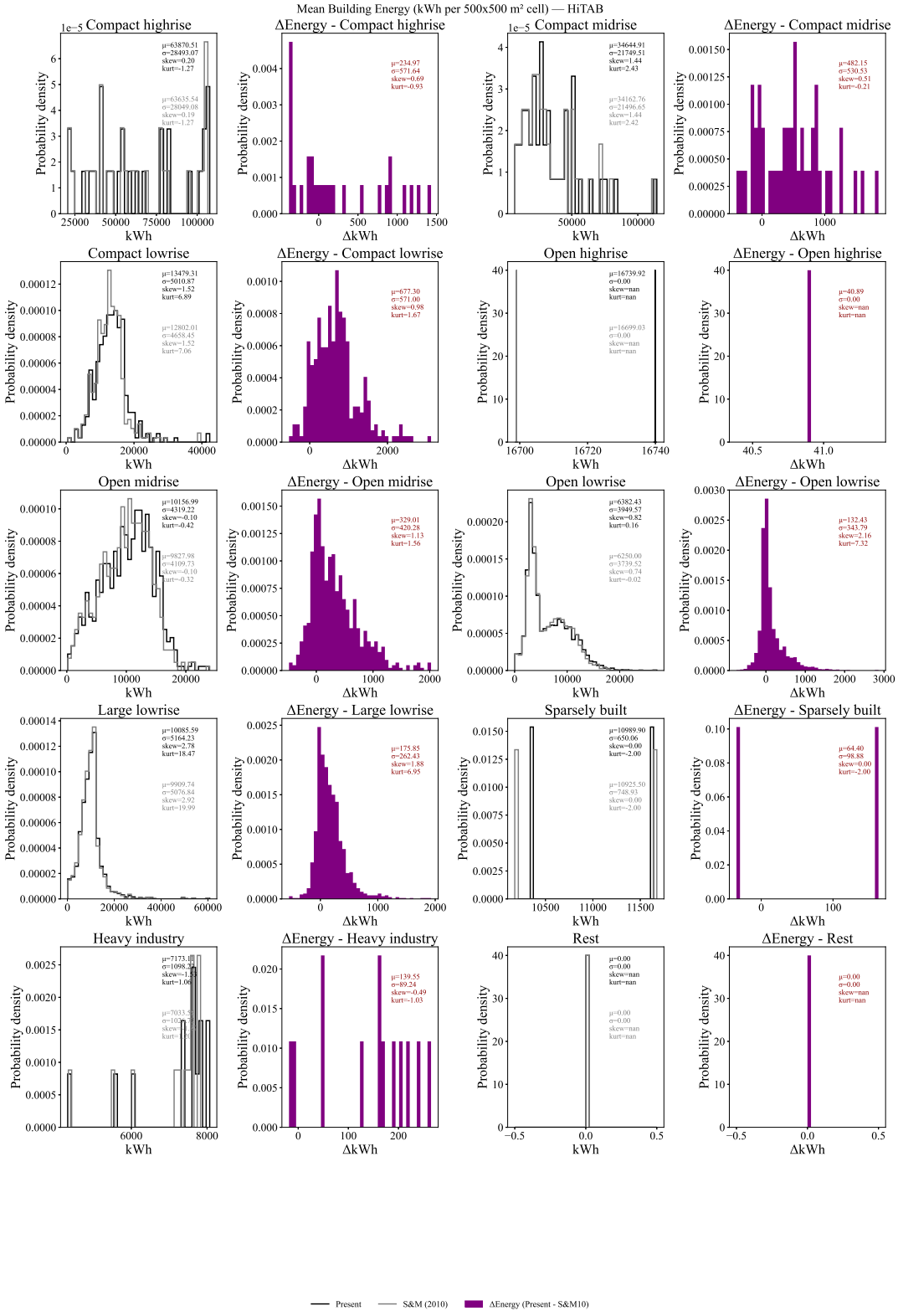

Fig. S18. Probability density functions (PDFs) of near-surface temperature (T) for different Local Climate Zones (LCZs), comparing the present study (black lines) and Santiago and Martilli (2010) (gray lines). Each row represents different LCZ categories. Middle panels show PDFs of the temperature differences (ΔT) between the two modeling approaches (present study minus Santiago and Martilli, 2010). Statistics displayed include mean (μ), standard deviation (σ), skewness (skew), and kurtosis (kurt).

References

1. JL Santiago, A Martilli, A dynamic urban canopy parameterization for mesoscale models based on computational fluid dynamics reynolds-averaged navier–stokes microscale simulations. *Boundary-Layer Meteorol.* **137**, 417–439 (2010).
2. A Simón-Moral, JL Santiago, ES Krayenhoff, A Martilli, Streamwise versus spanwise spacing of obstacle arrays: parametrization of the effects on drag and turbulence. *Boundary-Layer Meteorol.* **151**, 579–596 (2014).
3. N Nazarian, ES Krayenhoff, A Martilli, A one-dimensional model of turbulent flow through "urban" canopies (mlucm v2.0): updates based on large-eddy simulation. *Geosci. Model. Dev.* **13**, 937–953 (2020).
4. LP Blunn, et al., Turbulence characteristics across a range of idealized urban canopy geometries. *Boundary-Layer Meteorol.* **182**, 275–307 (2022).
5. T Nagel, R Schoetter, V Bourgin, V Masson, E Onofri, Drag coefficient and turbulence mixing length of local climate zone-based urban morphologies derived using obstacle-resolving modelling. *Boundary-Layer Meteorol.* **186**, 737–769 (2023).
6. S Whitaker, Theory and applications of transport in porous media: The method of volume averaging. *The Netherlands: Kluwer Acad. Publ.* **81** (1999).
7. N Nazarian, et al., Urbantales: A comprehensive les dataset for urban canopy layer turbulence analyses and parameterization development. (2025).
8. P Fischer, et al., Nekrs, a gpu-accelerated spectral element navier–stokes solver. *Parallel Comput.* **114**, 102982 (2022).
9. IP Castro, et al., Measurements and computations of flow in an urban street system. *Boundary-Layer Meteorol.* **162**, 207–230 (2017).
10. S Branford, O Coceal, T Thomas, S Belcher, Dispersion of a point-source release of a passive scalar through an urban-like array for different wind directions. *Boundary-Layer Meteorol.* **139**, 367–394 (2011).
11. ZT Xie, O Coceal, IP Castro, Large-eddy simulation of flows over random urban-like obstacles. *Boundary-layer meteorology* **129**, 1–23 (2008).
12. MO Deville, PF Fischer, EH Mund, *High-order methods for incompressible fluid flow.* (Cambridge university press) Vol. 9, (2002).
13. M Stuck, et al., Spectral-element simulation of the turbulent flow in an urban environment. *Appl. Sci.* **11**, 6472 (2021).
14. P Schlatter, S Stolz, L Kleiser, Les of transitional flows using the approximate deconvolution model. *Int. journal heat fluid flow* **25**, 549–558 (2004).
15. S Stolz, P Schlatter, L Kleiser, High-pass filtered eddy-viscosity models for large-eddy simulations of transitional and turbulent flow. *Phys. fluids* **17** (2005).
16. WC Skamarock, et al., A description of the advanced research wrf model version 4.3, (National Center for Atmospheric Research), Technical report (2021).
17. A Martilli, A Clappier, MW Rotach, An urban surface exchange parameterisation for mesoscale models. *Boundary-Layer Meteorol.* **104**, 261–304 (2002).
18. F Salamanca, A Martilli, A new building energy model coupled with an urban canopy parameterization for urban climate simulations—part ii. validation with one-dimension off-line simulations. *Theor. Appl. Climatol.* **99**, 345–356 (2010).
19. ES Krayenhoff, et al., A multi-layer urban canopy meteorological model with trees (bep-tree): Street tree impacts on pedestrian-level climate. *Urban Clim.* **32**, 100590 (2020).
20. H Hersbach, et al., The era5 global reanalysis. *Q. journal royal meteorological society* **146**, 1999–2049 (2020).
21. DJ Schwab, GA Leshkevich, GC Muhr, Satellite measurements of surface water temperature in the great lakes: Great lakes coastwatch. *J. Gt. Lakes Res.* **18**, 247–258 (1992).
22. J Wang, P Xue, W Pringle, Z Yang, Y Qian, Impacts of lake surface temperature on the summer climate over the great lakes region. *J. Geophys. Res. Atmospheres* **127**, e2021JD036231 (2022).
23. M Tewari, et al., Implementation and verification of the unified noah land surface model in the wrf model in *20th Conference on Weather Analysis and Forecasting/16th Conference on Numerical Weather Prediction.* pp. 11–15 (2004).
24. P Bougeault, P Lacarrere, Parameterization of orography-induced turbulence in a mesobeta–scale model. *Mon. weather review* **117**, 1872–1890 (1989).
25. SY Hong, JOJ Lim, The wrf single-moment 6-class microphysics scheme (wsm6). *J. Korean Meteorol. Soc.* **42**, 129–151 (2006).
26. J Dudhia, Numerical study of convection observed during the winter monsoon experiment using a mesoscale two-dimensional model. *J. Atmospheric Sci.* **46**, 3077–3107 (1989).
27. EJ Mlawer, SJ Taubman, PD Brown, MJ Iacono, SA Clough, Radiative transfer for inhomogeneous atmospheres: Rrtm, a validated correlated-k model for the longwave. *J. Geophys. Res. Atmospheres* **102**, 16663–16682 (1997).
28. ID Stewart, TR Oke, Local climate zones for urban temperature studies. *Bull. Am. Meteorol. Soc.* **93**, 1879–1900 (2012).
29. P Li, A Sharma, Detailed height mapping of trees and buildings (hitab) in chicago and its implications to urban climate studies. *Environ. Res. Lett.* **19**, 094013 (2024).
30. HG Kamath, et al., Global building heights for urban studies (ut-globus) for city-and street-scale urban simulations: development and first applications. *Sci. Data* **11**, 886 (2024).
31. M Demuzere, , et al., Combining expert and crowd-sourced training data to map urban form and functions for the continental us. *Sci. Data* **7**, 264 (2020).
32. Y Cheng, et al., U-surf: a global 1 km spatially continuous urban surface property dataset for kilometer-scale urban-resolving earth system modeling. *Earth Syst. Sci. Data* **17**, 2147–2174 (2025).

33. J O'Brien, et al., Crocus weather data at university of illinois-chicago tower, (Environmental System Science Data Infrastructure for a Virtual Ecosystem. Dataset.), Technical report (2024).
34. J O'Brien, et al., Crocus weather data at chicago state university prairie site, (Environmental System Science Data Infrastructure for a Virtual Ecosystem. Dataset.), Technical report (2024).